Ultrabroadband Dispersion of Third-Order Terahertz Nonlinearities

Supplementary Information

Binbin Zhou, Mattias Rasmussen, Siqi Yan[1], Narwan Noori, Oliver Nagy, Yunhong Ding, Simon Jappe Lange, Peter Uhd Jepsen*

Department of Electrical and Photonics Engineering, Technical University of Denmark, DK-2800 Kongens Lyngby, Denmark

**Corresponding author: puje@dtu.dk*

Contents

Determination of the nonlinear susceptibility of He and N_2 2

Length scaling of second-harmonic signal 3

Details on static THz-TDS of GaAs and SiO_2 5

Transmission measurements 5

Reflection measurements 5

Reflection spectroscopy of the GaAs TO phonon 6

Transmission spectroscopy of vibrational modes in SiO_2 thin films 8

Lorentz fit parameters for permittivity of SiO_2 9

Universal absorption in amorphous SiO_2 10

Basic characterization of the silicon nitride SSBCD device 11

Simulation of SSBCD device 12

Coherence length in SiO_2 17

Comparison between single-gap and five-gap electrode design 17

Lattice effects and diffraction in the SSBCD electrode structure 18

Supplementary references 20

[1] Current address: School of Optical and Electronic Information, Huazhong University of Science and Technology, Wuhan, China

Determination of the nonlinear susceptibility of He and N_2

The molecular dipole moment P_{mol} can be defined as

$$P_{mol} = \chi_{mol}^{(1)}E + \chi_{mol}^{(2)}E^2 + \chi_{mol}^{(3)}E^3 + \cdots . \tag{S1}$$

The third-order term in this expansion has three principal components. This can be seen with an input field that contains an oscillatory component at ω and a static component, $E = E_1 \cos\omega t + E_{dc}$,

$$\chi_{mol}^{(3)}E^3 = \frac{1}{4}\chi_{mol}^{(3)}\big(6E_1^2E_{dc} + 4E_{dc}^3 + (3E_1^3 + 12E_1E_{dc}^2)\cos\omega t + 6E_1^2E_{dc}\cos 2\omega t + E_1^3\cos 3\omega t\big) . \tag{S2}$$

Here we are interested in the term that causes an oscillating dipole moment at 2ω, with the standard notation $\chi_{mol}^{(3)}(-2\omega;\omega,\omega,0)$. The other terms correspond to the Kerr effect and third-harmonic generation. The SI units of $\chi_{mol}^{(3)}$ are $[\mathrm{C}^4\cdot\mathrm{m}^4\cdot\mathrm{J}^{-3}]$. In the more general situation where the static component is replaced with a low-frequency field that oscillates at a frequency Ω, the notation is $\chi_{mol}^{3}(-(2\omega\pm\Omega);\omega,\omega,\Omega)$.

The macroscopic nonlinear polarization density is often written as

$$P = \epsilon_0\big(\chi^{(1)}E + \chi^{(2)}E^2 + \chi^{(3)}E^3 + \cdots\big) , \tag{S3}$$

where ϵ_0 is the vacuum permittivity. The macroscopic polarization density is the molecular dipole moment times the density of the molecules. Thus, the relation between the molecular and the macroscopic third-order nonlinear susceptibility is

$$\chi^{(3)} = \frac{n}{\epsilon_0}\chi_{mol}^{(3)} . \tag{S4}$$

Using the ideal gas equation $pV = NRT$, the concentration $n = N/V$ at standard conditions ($P = 1\ \mathrm{bar}, T = 300\ \mathrm{K}$) is $n = 2.414\cdot 10^{25}\ \mathrm{m}^{-3}$.

Sitz and Yaris applied ab-initio theoretical methods [1] for the calculation of the frequency-dependence of the nonlinear susceptibilities of H_2 and He. Their results for the relevant third-order nonlinear susceptibility are shown as digitized data points (blue markers) in Figure S1a. The red curve is a phenomenological fit to the data, and the crosshair (black, dashed lines) indicate the value at a wavelength of 800 nm. The atomic units of third-order susceptibility are $1\ \mathrm{a.u.} = 6.2353\cdot 10^{-65}\mathrm{C}^4\cdot\mathrm{m}^4\cdot\mathrm{J}^{-3}$. Hence, we conclude that in SI units, the relevant third-order susceptibility of He gas at standard conditions is $\chi_{He}^{(3)}(-2\omega;\omega,\omega,0) = 7.55\cdot 10^{-27}\ \mathrm{m}^2\cdot\mathrm{V}^{-2}$.

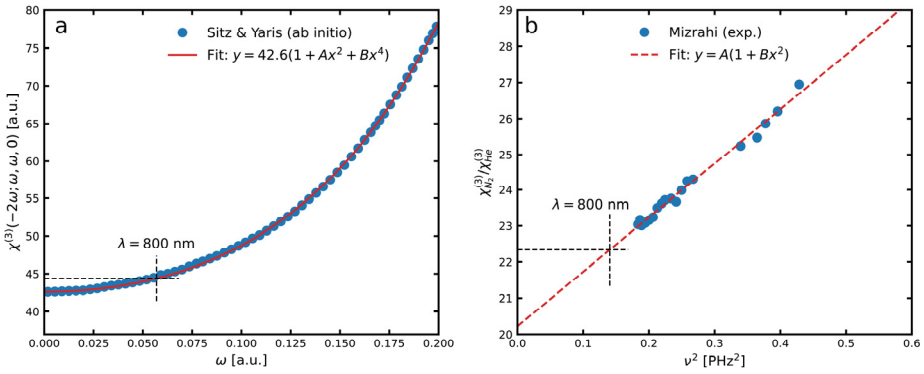

Figure S1. a) Blue markers indicate the third-order susceptibility $\chi^{(3)}(-2\omega;\omega,\omega,0)$ for He, as function of frequency (in atomic units), with digitized values from [1]. Red curve is a phenomenological fit. b) Ratio of the nonlinear susceptibilities of N_2 gas to He gas, experimental values from Mizrahi and Shelton [2] shown with blue markers together with a fit (red, dashed line).

Mizrahi and Shelton [2] later used electric-field-induced second-harmonic generation (ESHG) to measure the same component of the third-order nonlinear susceptibility for common gases, including N_2, relative to that of He. Their results are reproduced in Figure S1b. The original experimental data are shown as blue markers, and the dashed, red curve is a fit to the data. Combined with the known value for He, we find that in SI units, the third-order nonlinear susceptibility for N_2 gas at standard conditions is $\chi^{(3)}_{N_2}(-2\omega,\omega,\omega,0) = 22.34 \cdot \chi^{(3)}_{He}(-2\omega,\omega,\omega,0) = 1.686 \cdot 10^{-25}\ \mathrm{m^2 \cdot V^{-2}}$.

It is reasonable to assume that THz-frequency values of the nonlinear susceptibility of N_2 gas will be very close to this value, given that there are no strong rotational or vibrational resonances in the N_2 molecule across the relevant frequency range.

Length scaling of second-harmonic signal

The field-induced second-harmonic generation used in ABCD and SSBCD can be mathematically described by solving the nonlinear part of the wave equation. This leads to an expression for the intensity of the second-harmonic light generation that scales quadratically with the length of the dielectric medium. This result is well-known from second-harmonic generation by the second-order nonlinear susceptibility [3], but here we give a short summary of the derivation for the third-order nonlinearity relevant for TFISH.

The nonlinear wave equation describing the generation and propagation of the electric field due to the nonlinear polarization of the medium is

$$\frac{\partial^2 E(z,t)}{\partial z^2} - \frac{n^2}{c^2}\frac{\partial^2 E(z,t)}{\partial t^2} = \mu_0 \frac{\partial^2 P^{(3)}(z,t)}{\partial t^2} \tag{S5}$$

With an optical frequency ω of the input field, the third-order nonlinear polarization generates a signal at frequency 2ω when a DC field is applied as the third field. If the third field is a low-frequency (THz

frequency) field, the generated field will be at frequency $2\omega + \Omega$. Consequently, we seek for a solution for the THz-induced second-harmonic electric field $E_{2\omega+\Omega}$, and use the following definitions,

$$\begin{aligned} E_\omega(z,t) &= A_\omega(z)e^{ik_\omega z - i\omega t} \\ E_{THz}(z,t) &= A_\Omega(z)e^{ik_\Omega z - i\Omega t} \\ E_{2\omega+\Omega}(z,t) &= A_{2\omega+\Omega}(z)e^{ik_{2\omega+\Omega} z - i(2\omega+\Omega)t} \\ P^{(3)}(z,t) &= \epsilon_0\chi^{(3)}E_\omega^2(z,t)E_{THz}(z,t) \\ &= \epsilon_0\chi^{(3)}A_\omega^2 A_{THz}e^{i(2k_\omega+k_\Omega)z - i(2\omega+\Omega)t}\,. \end{aligned} \tag{S6}$$

Following the derivation of the Forward Maxwell Equation (FME) by Husakou and Herrmann [4] and assuming a harmonic time dependence of the fields so that $\partial/\partial t = -i\omega$ and $k(\omega) = n(\omega)\omega/c$, we write the operator on the field in the LHS of Eq. xx as $\partial^2/\partial z^2 + k^2 = (\partial/\partial z - ik)(\partial/\partial z + ik)$. The derivative of a forward-propagating plane wave $E(z) = E_0(z)e^{ikz}$ is $\partial E/\partial z = \big(\partial E_0/\partial z + ikE_0(z)\big)e^{ikz} \approx ikE_0(z)e^{ikz}$ where the last approximation is valid if $|\partial E_0/\partial z| \ll |kE_0|$, i.e. if the rate of change of the amplitude of the plane wave component is slow compared to the wavelength. In our specific scenario this approximation holds if the build-up of the second-harmonic intensity takes place over a distance corresponding to several wavelengths of the second-harmonic. The FME version of the wave equation is

$$\frac{\partial E(z)}{\partial z} - ikE(z) = -\frac{\mu_0\omega^2}{2ik}P^{(3)}(z)\,. \tag{S7}$$

We now solve this version of the wave equation for the generated field at $2\omega + \Omega$,

$$\begin{aligned} &\left(\frac{dA_{2\omega+\Omega}(z)}{dz} + ik_{2\omega+\Omega}A_{2\omega+\Omega}(z) - ik_{2\omega+\Omega}A_{2\omega+\Omega}(z)\right)e^{ik_{2\omega+\Omega}z} \\ &\qquad = -\frac{\mu_0\epsilon_0\omega^2\chi^{(3)}}{2ik}A_\omega^2(z)A_{THz}(z)e^{i(2k_\omega+k_\Omega)} \end{aligned} \tag{S8}$$

or, by removing terms that cancel each other and using $c = 1/\mu_0\epsilon_0$,

$$\frac{dA_{2\omega+\Omega}(z)}{dz} = \frac{i(2\omega+\Omega)\chi^{(3)}}{2n_{2\omega+\Omega}}A_\omega^2(z)A_{THz}(z)e^{i\Delta kz}, \tag{S9}$$

where $\Delta k = 2k_\omega - k_{2\omega+\Omega} + k_\Omega$.

If we make the additional simplification that the fundamental waves at ω and Ω are not depleted (i.e. A_ω and A_Ω are independent of z) then the solution to Eq. (S10) is

$$A_{2\omega+\Omega}(z) = \frac{(2\omega+\Omega)\chi^{(3)}}{2n_{2\omega+\Omega}\Delta k}A_\omega^2 A_{THz}\big(e^{i\Delta kz} - 1\big) \tag{S10}$$

In the limiting case of good phase matching ($\Delta kz \ll 1$) the solution for the amplitude of the second-harmonic field reduces to

$$A_{2\omega+\Omega}(z) = \frac{(2\omega+\Omega)\chi^{(3)}}{2n_{2\omega+\Omega}} A_{\omega}^2 A_{THz} \cdot z\,. \tag{S11}$$

Thus, the intensity of the THz-induced second-harmonic signal will increase as

$$I_{2\omega+\Omega}(z) \propto |A_{2\omega+\Omega}(z)|^2 \propto \left(\chi^{(3)} I_{\omega}\right)^2 A_{\Omega}^2 z^2 \tag{S12}$$

Hence, the intensity of the THz-induced second-harmonic light increases to a good approximation quadratically with the length of the nonlinear medium as predicted also for regular, non-depleted second-harmonic generation in a $\chi^{(2)}$ medium. We expect this to be the case both for nitrogen plasma, SiO_2 and SiN.

Details on static THz-TDS of GaAs and SiO_2

Transmission measurements

A bulk transmission experiment is analyzed by the well-known equations for single-pass transmission [5],

$$\begin{aligned} n(\omega) &= 1 + \frac{c\Delta\phi}{\omega d}\,, \\ \alpha(\omega) &= -\frac{2}{d}\ln\left(\frac{(n(\omega)+1)^2}{4n(\omega)}|T(\omega)|\right), \end{aligned} \tag{S13}$$

where $\Delta\phi(\omega)$ is the phase difference between sample and reference, $|T(\omega)|$ is the amplitude ratio between the sample and the reference, d is the sample thickness, and $\omega = 2\pi\nu$ is the angular frequency.

In the case of a thin film of finite thickness d on a substrate, the multiple reflections in the film must be taken into account as described in many optics textbooks [6]. If the substrate refractive index is n_{sub} then the ratio between the sample and the reference is

$$T(\omega) \equiv |T(\omega)|e^{i\Delta\phi} = \frac{\frac{2n(n_{sub}+1)}{(n+1)(n+n_{sub})}e^{i\delta}}{1-\frac{(n-n_{sub})(n-1)}{(n+n_{sub})(n+1)}e^{2i\delta}}, \tag{S14}$$

where $n = n_r + in_i$ is the complex index of refraction of the thin film and $\delta = \omega n d/c$ is the single-trip phase accumulated by the plane wave through the film. This equation cannot be inverted analytically, so the solution to n must be found by numerical minimization methods. The complex-valued index of refraction can be used to calculate the permittivity, $\epsilon(\omega) = n(\omega)^2$, and the conductivity, $\sigma(\omega) = -i\epsilon_0\omega(\epsilon(\omega) - \epsilon_\infty)$ where ϵ_∞ is the background permittivity at high frequencies of the material and ϵ_0 is the vacuum permittivity.

Reflection measurements

In a similar manner, a reflection measurement on a bulk sample, using a reference surface with a known reflection coefficient $r_{ref}(\omega)$, can be analyzed based on the measured reflection ratio $r(\omega) =$

$|r(\omega)|e^{i\Delta\phi}$ between sample and reference. Calibrated reflection measurements are notoriously difficult to perform, and in practice a correction factor taking unintended, minor misalignment between the sample and reference reflections is required for consistent results. If the calibration factor is $K = |K|e^{i\omega\Delta t}$, then the refractive index can be extracted from a normal-incidence measurement as

$$n(\omega) = \frac{K + r}{K - r}. \tag{S15}$$

In an ideal measurement, $K = 1$. However, small amplitude deviations from unity of the calibration factor ($|K|$) can account for unintended, minute angle deviations between sample and reference. The absolute reflectivity r_{ref} of a highly reflecting reference surface can be difficult to determine with absolute accuracy. The noble metals (Au, Ag, Cu) have high conductivities, and using a reasonable Drude scattering time of 10 fs, the theoretical reflection coefficient across the THz range of these metals is very close to unity within 0.1% to 0.5% in the range from 0 to 35 THz. Hence, for practical purposes it may be assumed that $r_{ref} \approx -1$ if a plane, polished metal surface is used for the reference reflection.

If the plane of reflection for the sample and the reference measurements is displaced slightly by an amount Δx due to the thickness of the film or unintentional misalignment during displacement between the two measurements, the sample signal will be delayed artificially by an amount $\Delta t = 2\Delta x/c$. This shift corresponds to a frequency-dependent phase shift $\delta\phi = \omega\Delta t$. In practice, a small shift of this kind is extremely difficult to avoid, and it will influence the precision of the subsequent determination of the complex-valued refractive index of the sample. However, the effect of the unintentional phase shift can be included in the analysis by noting that the strictly linear dependence on frequency can be identified as a slope on the phase difference between sample and reference. Such a slope cannot be caused by the response (e.g. Drude, Debye, Lorentz) of the material, and hence it can be corrected in the data extraction procedure.

Reflection spectroscopy of the GaAs TO phonon

Measurements were performed with a temporal step size of 3.33 fs (0.5 μm displacement) over a time window of 10 ps. Figure S2a shows the first part of the time traces from the reference (blue curve) and sample (orange curve) measurements. Figure S2b and c show the spectral intensities and phases of the two signals. The amplitude ratio $|r(\omega)|$ and phase difference $\Delta\phi(\omega)$ are shown in Figure S2d and e, respectively. The data consists of two reference scans and four sample scans, measured in sequence over a duration of approximately two hours. The light blue and orange bands indicate the standard deviation of the data based on averaging of the individual traces. The phase difference in Figure S2e sits on a slope marked by the black, dashed line. As will be discussed below, this slope is due to an unintentional shift of the reflection plane when shifting between the sample and reference positions. The useful spectroscopic range is approximate 1 – 20 THz. The Reststrahlen band of high reflection and rapid phase variation between the TO and the LO phonon is clearly visible.

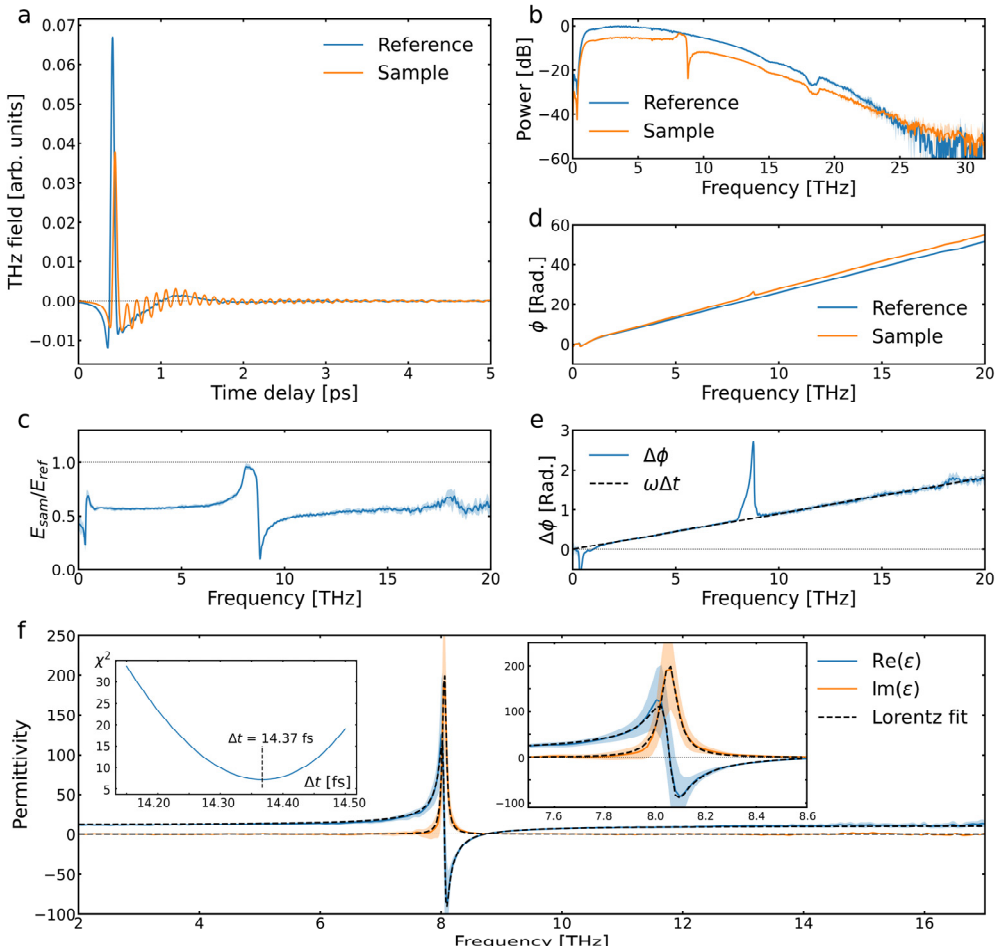

Figure S2. THz reflection spectroscopy. (a) Time-domain traces of reference (blue curve, gold reference surface) and sample (orange curve, GaAs surface) THz transients. (b) Spectral power and (c) optical phase of the reference and sample signals. (d) Transmission ratio and (e) phase difference between sample and reference signals. The dashed line indicates the phase correction due to unequal path lengths of the sample and reference pulses. (f) Extracted real (blue curve) and imaginary (orange curve) permittivity of GaAs. Dashed lines represent a best fit with the Lorentz model. Light blue and orange bands indicate the experimental standard deviation of the measurement.

The permittivity is calculated by Eq. (S16) followed by conversion of the resulting refractive index to permittivity, and the result is shown in Figure S2f. The real and imaginary parts of the permittivity are shown as blue and orange curves, respectively. The light-colored bands indicate the standard deviation of the calculated permittivity, based on error propagation through the underlying equations. The inset to the right in Figure S2f shows the region close to the TO phonon.

The black, dashed curves in Figure S2f represent a fit of the Lorentz oscillator model to the experimental data,

$$\epsilon(\omega) = \epsilon_\infty + \frac{A}{\omega_{TO}^2 - \omega^2 - i\omega\Gamma}, \tag{S16}$$

Where ω_{TO} is the resonance frequency, Γ is the damping rate, and A is the oscillator strength. The fit is excellent, and is based on the best-fit parameters $\epsilon_\infty = 10.99 \pm 0.08,\ A = (4897 \pm 32)\ \mathrm{ps}^{-2}, \omega_0 =$

$(50.607 \pm 0.002)\mathrm{ps}^{-1}, \Gamma = (0.471 \pm 0.004)\ \mathrm{ps}^{-1}$. The uncertainties indicate the 95% confidence intervals. The oscillator strength is related to the overall change of the real part of the permittivity across the resonance, $\Delta\epsilon = A/\omega_{TO}^2 = 1.912 \pm 0.012$. The LO frequency can be estimated via $A = \epsilon_\infty(\omega_{LO}^2 - \omega_{TO}^2)$ so that $\omega_{LO} = 54.83\ \mathrm{ps}^{-1}$ (8.727 THz). The damping rate corresponds to a decay time $\tau = 1/\Gamma = 2.12$ ps.

We need to take the unintentional displacement between the sample and reference plane of reflection into account to obtain a good fit between the Lorentz model and the experimental results. In principle, as discussed above, the residual slope of the phase difference between sample and reference measurements could be removed blindly, but we have followed a procedure where the temporal offset was varied over a relevant range, and the calculation of the permittivity and subsequent fitting was performed. The reduced χ^2 value of the fit was recorded for each offset time, and the position with the smallest χ^2 was then chosen as the optimal value for the unintentional delay between the reflected reference and sample time traces. The result of this procedure is shown in the inset to the left in. An optimal time delay of $\Delta t = 14.37$ fs was then used in the final data analysis. This time shift corresponds to an unintended displacement of $\Delta x = 2.15\ \mu$m between the two reflection planes. The slope shown in Figure S2e as a black, dashed line, is calculated based on this value, and it coincides very well with the visually expected background slope of the phase difference. We find that using other values for Δt results in significant disturbances of the calculated permittivity (not shown here), so even very minor errors in the positioning of the sample will lead to unpredictable results in reflection-type THz-TDS, unless corrected for. Additionally, we used a slight amplitude correction ($|K| = 1.02$ in Eq. (S15)) to reproduce the value $\epsilon(0) = 12.9$ for the static permittivity of GaAs.

Transmission spectroscopy of vibrational modes in SiO_2 thin films

The spectroscopic investigation follows the same pattern as described above for measurement of the permittivity of GaAs. Here we use a thin film of SiO_2 on a high-resistivity silicon (Si) wafer, formed by controlled oxidation. The thickness of the film is 1.879 µm, measured by a profilometer. We subsequently removed the oxide layer on one half of the wafer so that a sample and reference area was available on the same wafer. Measurements were performed in transmission, and the sample was placed in the parallel section of the THz beam before the intermediate focus. Figure S3a shows the time traces of the THz transients transmitted through the Si wafer (blue curve) and through the SiO_2 film on the wafer (orange curve). Figure S3b and c show the spectral intensity and the phases of the two pulses, respectively, and Figure S3d+e show the amplitude ratio $|T(\omega)|$ and phase difference $\Delta\phi(\omega)$ between sample and reference signals. As before, the light-colored bands indicate the standard deviation of the measurements, here based on two reference scans and two sample scans recorded within one hour. In this case, the useful bandwidth extends to beyond 30 THz, slightly higher than in the case of GaAs. This additional spectral coverage is most likely due to better imaging of the THz beam through the

arrangement of off-axis paraboloidal mirrors that in transmission geometry is optimally arranged. In reflection geometry the reflected beam travels a longer distance than $2f$ between the two last mirrors, and although the beam is nominally collimated, the imaging properties of the optical setup is slightly degraded.

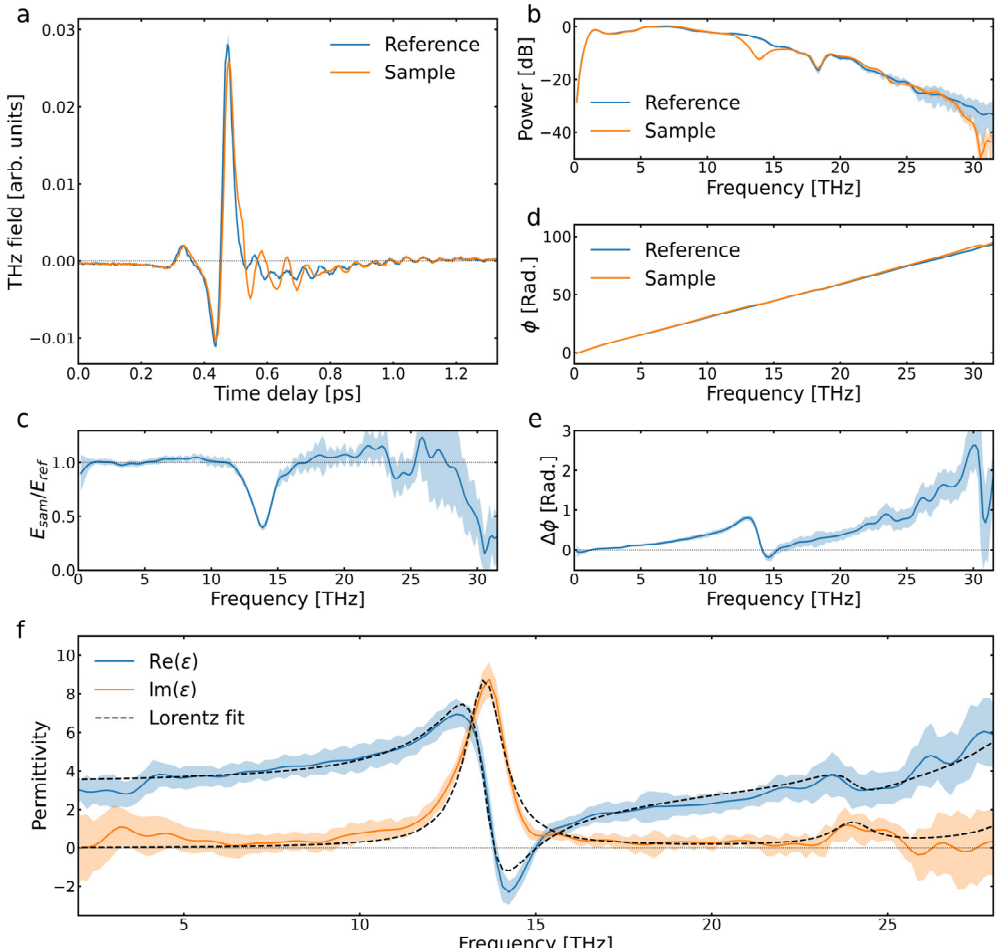

Figure S3. (a) Time-domain traces of reference (blue curve, Si substrate) and sample (orange curve, 1.87 µm SiO_2+Si substrate) THz transients. (b) Spectral power and (c) optical phase of the reference and sample signals. (d) Transmission ratio and (e) phase difference between sample and reference signals. (f) Extracted real (blue curve) and imaginary (orange curve) permittivity of the SiO_2 film. Dashed lines represent a best fit using three Lorentz oscillators. Light blue and orange bands indicate the experimental standard deviation between scans.

We then used Eq. (S14) to find the complex index of refraction and subsequently the permittivity of the SiO_2 film, with $n_{sub} = 3.4177$ [7]. The real and imaginary parts of the extracted permittivity is shown in Figure S3f as blue and orange curves, respectively. The associated standard deviations are indicated by correspondingly colored bands.

Lorentz fit parameters for permittivity of SiO_2

The best-estimate parameters for the Lorentzian fit to the measured permittivity of SiO2 shown in the main article are listed in Table S1.

We use the fit to the experimental data in the FEM simulations of the SSBCD device.

Table S1: Lorentz fit parameters for the fit in **Error! Reference source not found.** in the main particle (SiO_2). Parameters for the first resonance are based on a fit to the vibrational feature at 14 THz, the remaining entries have been manually adjusted.

Parameter	Units	Value
A_0	[ps^{-2}]	$(5.98 \pm 0.21) \cdot 10^3$
$\omega_{TO,0}$	[ps^{-1}]	85.2 ± 0.13
$\omega_{LO,0}$	[ps^{-1}]	101.8
$\Delta\epsilon_0$		0.82
Γ_0	[ps^{-1}]	8.06 ± 0.39
A_1	[ps^{-2}]	$1.5 \cdot 10^3$
$\omega_{TO,1}$	[ps^{-1}]	151
$\omega_{LO,1}$	[ps^{-1}]	153.6
$\Delta\epsilon_1$		0.066
Γ_1	[ps^{-1}]	8.9
A_2	[ps^{-2}]	$2.7 \cdot 10^4$
$\omega_{TO,2}$	[ps^{-1}]	193
$\omega_{LO,2}$	[ps^{-1}]	226
$\Delta\epsilon_2$		0.72
Γ_2	[ps^{-1}]	9.7
ϵ_∞		1.929

Universal absorption in amorphous SiO_2

The absorption coefficient of a wide range of amorphous materials is known to follow a universal law of the form $\alpha(\nu) = K\nu^\beta$, where β is a scaling exponent. This universal behavior can be expected in the frequency range below the isolated vibrational modes of the amorphous material. Figure S4 shows a separate measurement of the absorption coefficient of a bulk sample of fused silica. Measurements in the low-frequency (< 2 THz) range were performed with a commercial THz system using photoconductive antennas (PCA), and the high-frequency (> 2 THz) was covered by the ABCD technique. We observe the universal scaling behavior, with an exponent $\beta \approx 1.9$. This confirms the molecular dynamics results by Taraskin *et al.* [8] predicting a universal behavior of the coupling between IR photons and atomic vibrations of the form $C(\omega) = A + B\omega^2$ over an unprecedented frequency range. The cross-over from the universal behavior to located vibrations in SiO_2 is approximately at 8 THz.

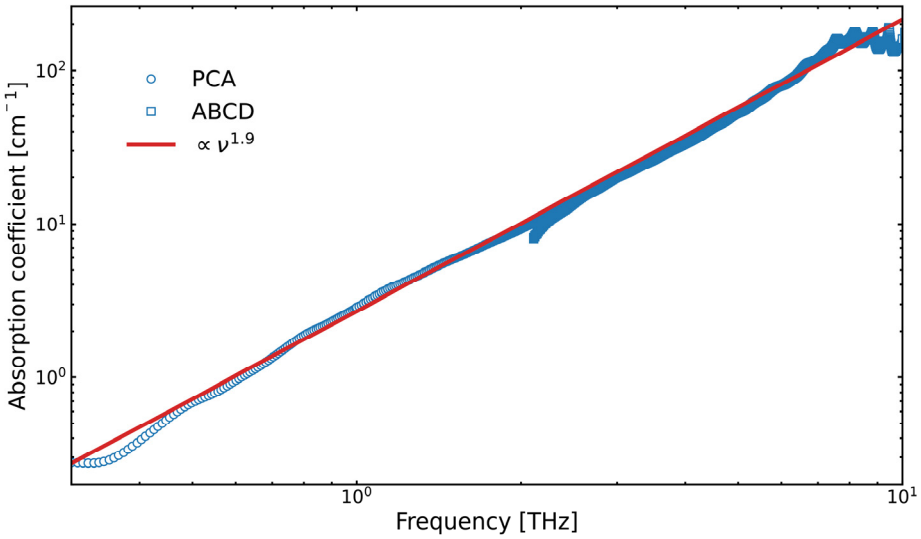

Figure S4. Double-logarithmic plot of the absorption coefficient of bulk fused silica (thickness 1 mm) measured with a PCA-based commercial setup (0.1 – 2 THz) and our ABCD setup (2-10 THz). The red line is a power-law with exponent 1.9.

Basic characterization of the silicon nitride SSBCD device

General characterization of the basic functionality of the SSBCD detector includes the dependency of the detection signal on bias voltage, THz field strength, and optical probe intensity. The characterization of our SiN-based SSBCD device discussed in the main article. The measurements show quadratic dependence on the optical probe pulse energy, and linear dependence on both the bias and THz power, which agree very well with the lock-in-based heterodyne biased coherent detection mechanism that predicts $I_{2\omega} \propto \left(\chi^{(3)} I_{\omega}\right)^2 E_{bias} E_{THz}$. This dependence has also been verified in earlier SSBCD works [9, 10], and here we show the results obtained on our device. Very similar results (not shown) are obtained on our SiO2-based devices.

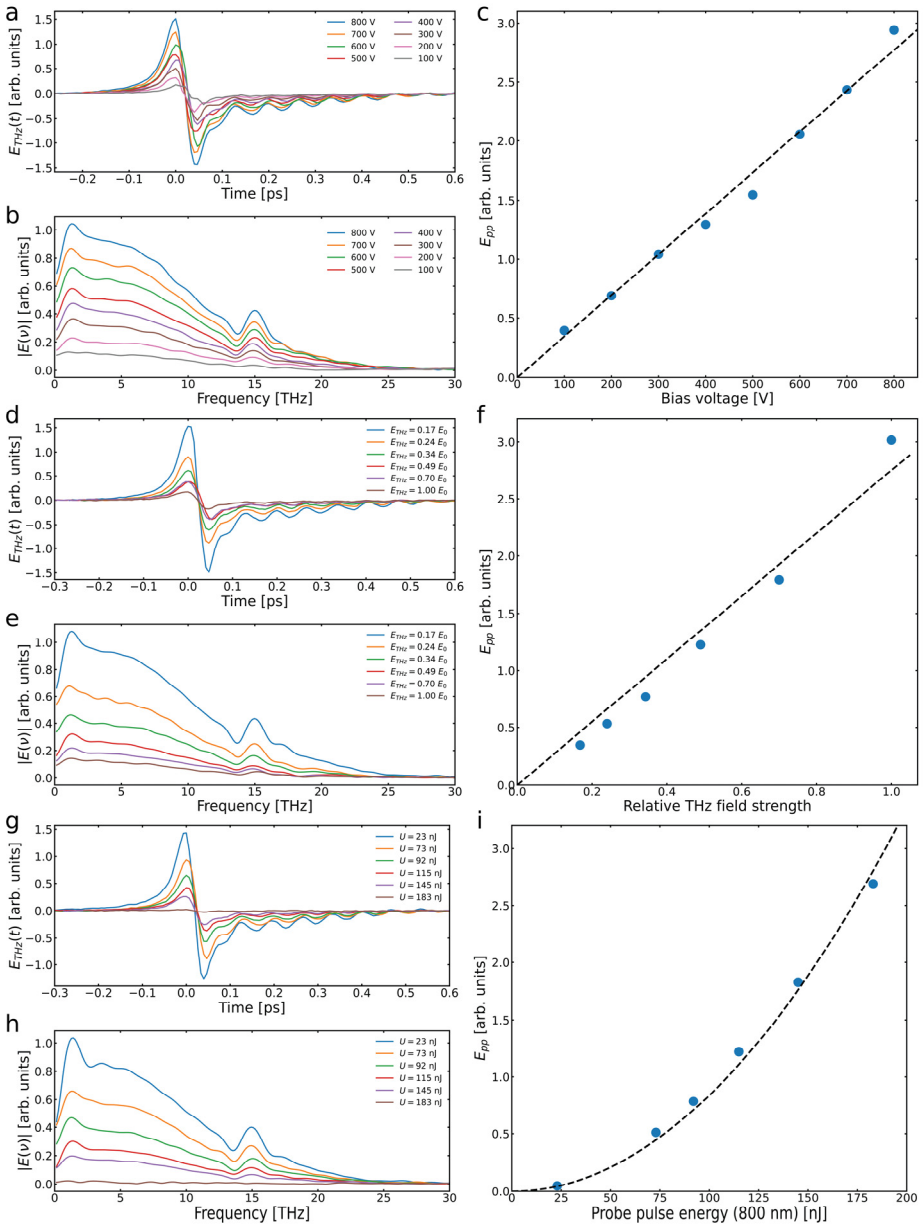

Figure S5. General characterizations of the SiN solid-state detector performance with respect to bias voltage (a,b,c), THz field strength (d,e,f) and optical probe energy (g,h,i). For each series the THz time traces (a,d,g), the corresponding amplitude spectra (b,e,h) are shown. The bias voltage sweep (c) was performed with 250 nJ THz pulse energy and 183 nJ optical probe energy. The THz field strength sweep (f) was swept from 0-100% of 250 nJ pulse energy with optical probe energy 183 nJ and 800 V total bias voltage. The probe pulse energy sweep was recorded with 250 nJ THz pulse energy and 800 V total bias voltage.

Simulation of SSBCD device

As discussed in the main article, the intensity of the THz-induced second-harmonic signal in ABCD and SSBCD scales as $I_{2\omega} \propto \left(\chi^{(3)} I_{\omega}\right)^2 E_{bias} E_{THz}$. For a spatially varying environment, the full signal will be the result of an integration over the emission area,

$$I_{2\omega} \propto \int_x \left(\chi^{(3)} I_\omega(x)\right)^2 E_{bias}(x) E_{THz}(x) dx \,. \tag{S17}$$

Since the SSBCD device is composed of narrow gold electrodes separated by dielectric gaps, it is important to estimate the effects of inhomogeneous field distributions and possible field enhancement in the structure.

We use the finite element software Comsol to simulate the electromagnetic properties of the 6-electrode SSBCD structure shown in the main article. The long electrodes allow us to reduce the simulation problem to 2 dimensions. The gold electrodes are 2 μm wide and 240 nm high, and the material is described by a Drude model with a DC conductivity of $4.7 \cdot 10^7$ S/m and an electron scattering time of 10 fs. The spacing between the electrodes is 10 μm, and they are covered by a 1 μm amorphous SiO_2 layer and is placed on a semi-infinite amorphous SiO_2 substrate. The dielectric properties of the SiO_2 in the THz range and at DC are taken from the fit presented above and in the main article. We use periodic boundary conditions in the horizontal (x) direction, scattering boundary conditions in the vertical (y) direction, and the source is a plane wave with field strength 1 V/m, incident from the air side in the $-y$ direction normal to the interface, and polarized in the x direction. The simulation mesh is refined in the narrow regions, as shown in Figure S6. The simulation area contains approximately $3.2 \cdot 10^5$ mesh elements. For simulation of the SiN-based SSBCD detector, we replaced a 500-nm thick layer of the SiO_2 cap with SiN. The model dielectric properties of SiN was the frequency-dependent permittivity shown in Figure S10b.

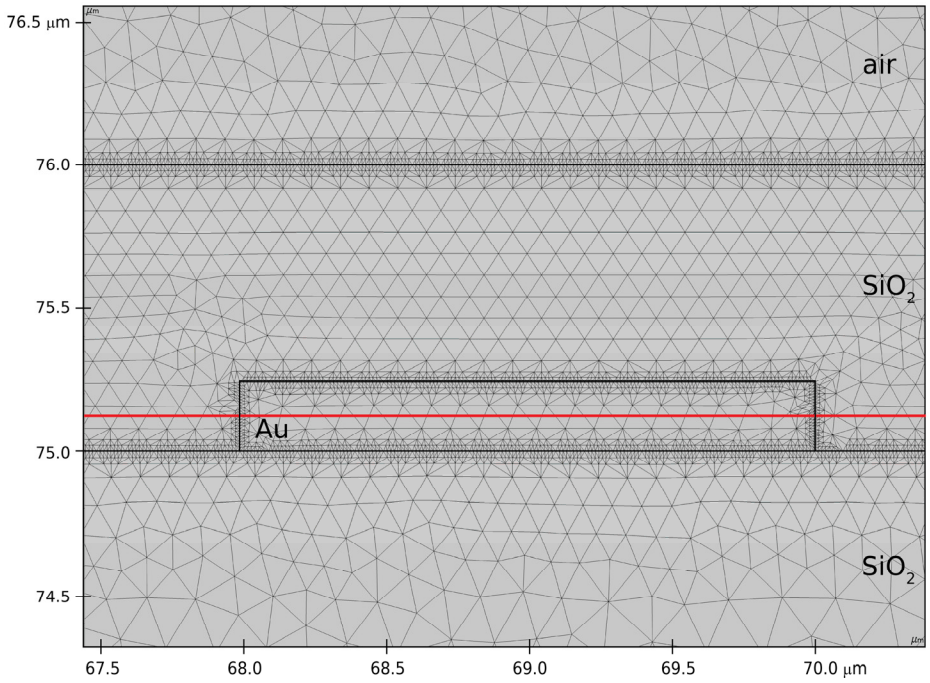

Figure S6. Example of meshing in the static and THz-frequency finite element simulations. The image shows the refined mesh surrounding one of the gold electrodes. The same mesh was used in electrostatic and THz-

frequency simulations. The red line indicates the path where the electrostatic potential, the DC bias, and the THz electric fields are evaluated.

First, we performed an electrostatic simulation to confirm the DC potential and electric field ($E_{bias}^{SiO_2}$) between the electrodes. When setting the electrodes at potentials $V = (100, 80, 60, 40, 20, 0)$ V, the electrostatic potential and the static electric field was calculated along a horizontal line across all electrodes, as indicated in Figure S6 (red line). The electrostatic potential is shown in Figure S7a, and the electric field between the electrodes is shown in Figure S7b. Due to the finite geometry and small height/width ratio of the electrodes, the electric field is not constant between the electrodes. However, as expected the average electric field between each electrode is identical to the potential difference divided by the distance ($20\text{V}/10\ \mu\text{m} = 2\text{V}/\mu\text{m}$), indicated in red in Figure S7b.

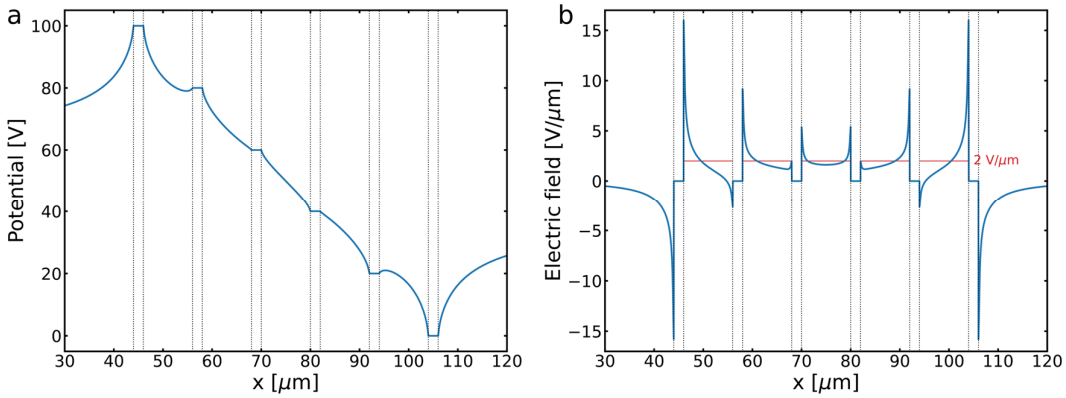

Figure S7. (a) Electrostatic potential and (b) horizontal DC bias field across the six electrodes. The potential on the electrodes (from left to right) is 100V, 80V, 60V, 40V, 20V and 0V.

Next, we simulated the distribution of the 800-nm probe beam in the vicinity of the electrodes. We used a permittivity of SiO_2 of 2.112 and a complex-valued refractive index of gold of $0.1886 + 4.7053i$, and a maximum mesh spacing of $\lambda/20$. The absolute value of the horizontal component of the electric field of the probe is shown in Figure S8a. The full spatial distribution of this field component is shown in Figure S8b. The shadow zone of the metal electrode is clearly visible, together with the reflected field above the electrode and diffraction into the shadow zone due to the small dimensions of the electrode. However, we observe no significant field enhancement at the edges of the electrodes. Hence we can treat the intensity of the probe beam as constant between the electrodes.

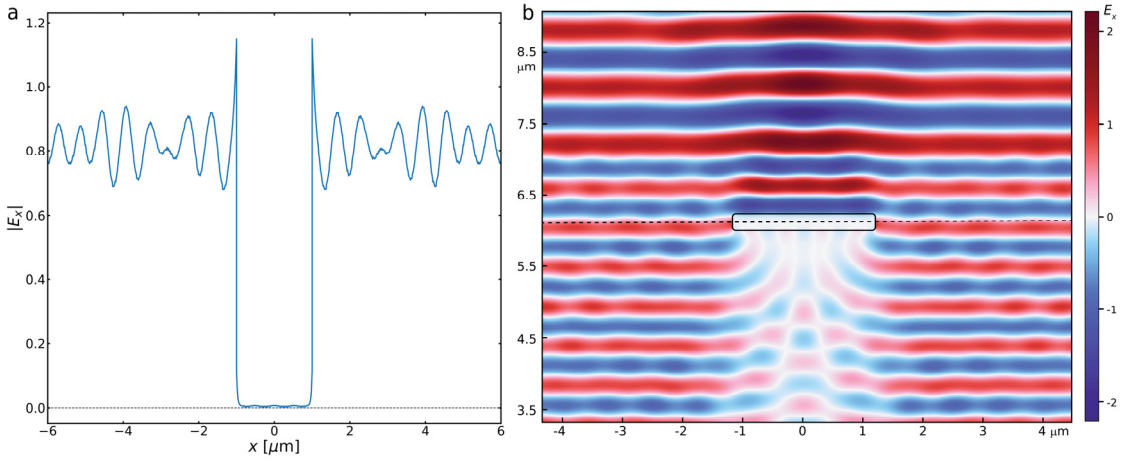

Figure S8. (a) Horizontal component of the electric field of the probe laser light incident on one of the electrodes. The wavelength is 800 nm. (b) Distribution of the electric field of the probe laser beam in the vicinity of the metal electrode.

Finally, we performed THz-frequency simulations of the structure in the frequency range 1 – 40 THz. The field distribution near one of the electrodes is shown in Figure S9a, for selected frequencies 1 (blue curve), 10 (orange curve) and 40 THz (green curve). The incident field strength is 1 V/m. A moderate field enhancement close to the electrode edges is seen at all frequencies. The absolute field strength is largely determined by frequency-dependent permittivity of SiO_2 (see below). Figure S9b compares the distribution of the bias field (green curve), the THz field at 10 THz (orange curve) and the probe field at 800 nm (blue curve).

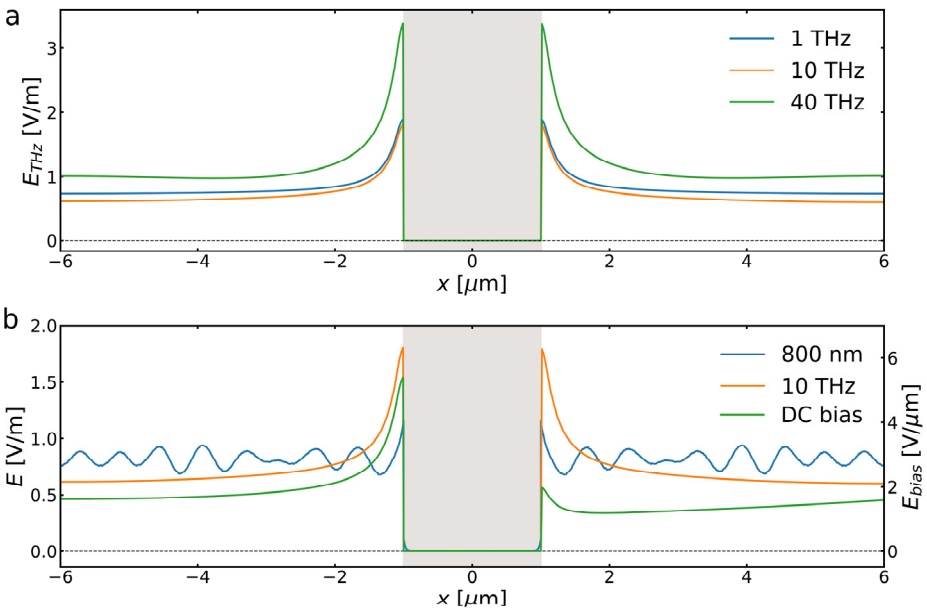

Figure S9. (a) Field enhancement of the horizontal component E_x of the THz field incident on the SSBCD device near one of the electrodes, shown for frequencies 1, 10 and 40 THz (blue, orange and green curves, respectively). (b) Comparison of field enhancement near an electrode for the DC bias field (green curve), at 10 THz (orange curve) and at 800 nm (blue curve).

The frequency dependence of the average THz field strength in the gaps is shown below (Figure S10c+d). The combined effect of the geometry of the electrode structure on the distribution of the DC bias field and the 800 nm probe field is a modest 5% enhancement of the second-harmonic generation.

Figure S10a+b show the model permittivity functions of amorphous SiO_2 and SiN used in the simulations in the 1 – 40 THz range. SiN data are from Tice *et al.* [11] and Cataldo *et al.* [12]. Tice *et al.* applied ellipsometry on CVD-grown films and applied the Bruggeman effective medium theory with 50% voids in their fitting. Cataldo *et al.* used Fourier-Transform Infrared (FTIR) spectroscopy in transmission on free-standing SiN films grown by LP-CVD with focus on low-stress films, and the transmission spectrum was fitted with a multi-Lorentz model with frequency-dependent linewidths. The results of the two studies are comparable, with indication of variation e.g. between the low-frequency value of the permittivity. The dominant absorption bands are at 13-16 THz and 23-29 THz (strongest).

Figure S10c+d shows the simulated field strength as function of frequency, averaged across the central gap of the SSBCD structure (blue curve) and at the same depth (880 nm) in bulk, away from the electrode structure (SiO_2 in Figure S10c and SiN in Figure S10d) and in SiN As above, the simulations are performed with an incident field strength of 1 V/m. We observe a relative enhancement of the local field in the range 15-20 THz and 35-40 THz. We use this local field strength relative to that of the incoming THz wave in the evaluation of the effective $\chi^{(3)}$ of SiO_2 in the main article.

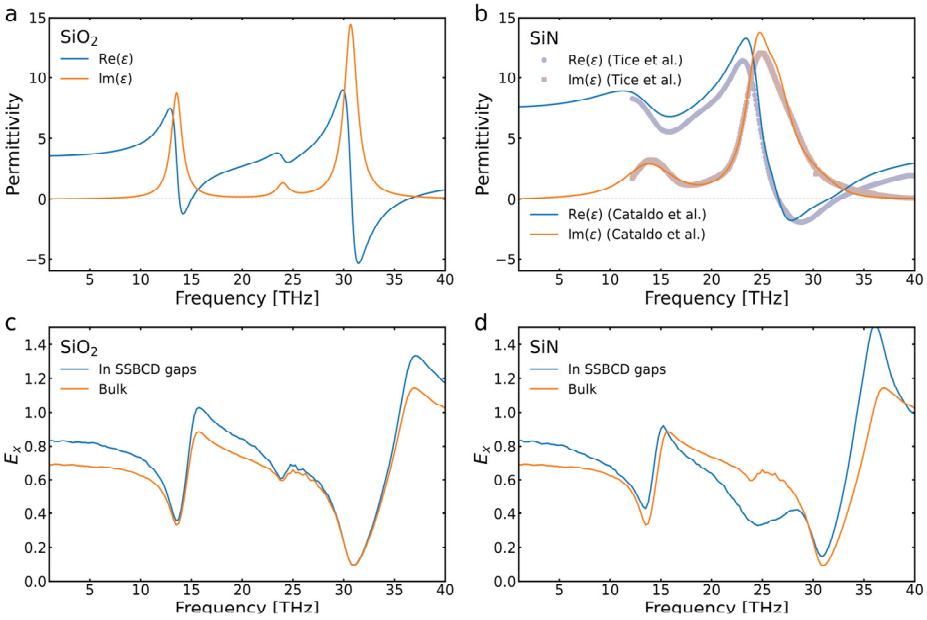

Figure S10. (a) Model permittivity function of amorphous SiO_2 as derived from the ABCD THz-TDS measurements in the main article. (b) Simulated frequency-dependent average field strength (E_x) across the central gap at the depth of the electrodes in the SiO_2 SSBCD detector (blue curve) and at the same depth in bulk, amorphous SiO_2 (orange curve).

Coherence length in SiO_2

The coherence length between an optical probe pulse and the propagating THz field is calculated as

$$L_{coh} = \frac{\pi}{|k_{2\omega} - 2k_{\omega} - k_{\Omega}|} = \frac{\pi c}{2\omega|n_{2\omega} - n_{g,\omega} - n_{\Omega}\Omega/2\omega|} \quad \text{(S18)}$$

where $n_{g,\omega}$ is the group index at the probe wavelength, $n_{2\omega}$ is the refractive index at the second harmonic, and n_{Ω} is the refractive index at THz frequency Ω. Using $n_{g,\omega} = 1.4671\ (2.0778)$ and $n_{2\omega} = 1.4701\ (2.1004)$ for the group index of fused silica (silicon nitride) at 800 nm wavelength and the phase index at 400 nm[2], we find that the build-up of the second-harmonic signal in general takes place during the first 1 μm of the glass, and hence we have used this distance as the interaction length in SiO_2 in the calculation of $\chi^{(3)}$ of SiO_2, and the film thickness (500 μm) in the calculation of $\chi^{(3)}$ for SiN, taking into account that the SiN layer is below a 500-nm SiO_2 top layer. The coherence length as well as the penetration depth of the THz field into the glass can be expected to vary significantly with frequency due to the dispersion of the refractive index of the glass across the THz range, the frequency dependence of the phase matching conditions will not be investigated further here.

Comparison between single-gap and five-gap electrode design

The five-gap electrode structure that we have applied has two main advantages compared to a design with a single gap across the same total width of the electrode area. Figure S11 shows a comparison of FEM simulations of the electrostatic properties of the two electrode geometries (shown in the inset of Figure S11a). In both cases, a potential of 100 V is applied to the left-most electrode, and the right-most electrode is grounded. Figure S11a show the electrostatic potential on a horizontal line (x direction) through the electrode region, and Figure S11b shows the corresponding horizontal component of the electric field E_x. The most important difference between the two designs in the confinement of the electric field in the vertical (y) direction, as shown in Figure S11c. The five-gap structure features a better confinement of the bias field to the relevant electrode region, resulting in a higher bias field in the gap region.

[2] Values obtained from https://refractiveindex.info/

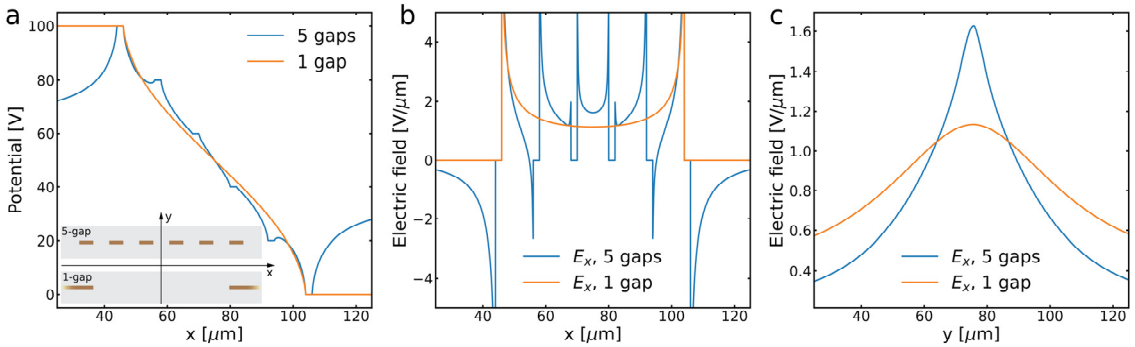

Figure S11. Comparison of electrostatic characteristics of the five-gap electrode design used in this investigation and a design with a single gap with the same area. (a) Electrostatic potential in the gap region with a potential of 100 V at the left electrode and 0 V at the right electrode. The inset shows schematic cross-section of the 5-gap and 1-gap electrode geometries. (b) Electric field (E_x) in the gap region (horizontal cross-section). (c) Electric field (E_x) in the vertical direction, central

Lattice effects and diffraction in the SSBCD electrode structure

We observe two interesting, but predictable effects in the simulation of the interaction between the incoming THz field and the electrode structure of the SSBCD. Firstly, we see in Figure S10b that the real part of the permittivity is negative in the regions 14-15 THz and 31-36 THz. Hence, the SiO2 surface should be able to support surface phonon-polariton modes in these frequency bands. The FEM simulations confirm this. Figure S12 shows a series of density plots of the out-of-plane E_y field components in the 13.75 – 15.00 THz range. We see the excitation of the phonon-polariton mode in this range, strongest at 14.5 THz. The excitation happens over the electrodes buried in the SiO_2 due to the diffraction of the incoming plane wave that creates a localized out-of-plane field component with sufficiently large in-plane momentum to excite the phonon-polariton mode. The same effect is seen in the higher frequency band, as shown in Figure S13. Additionally, we see significant far-field diffraction from the array of electrodes.

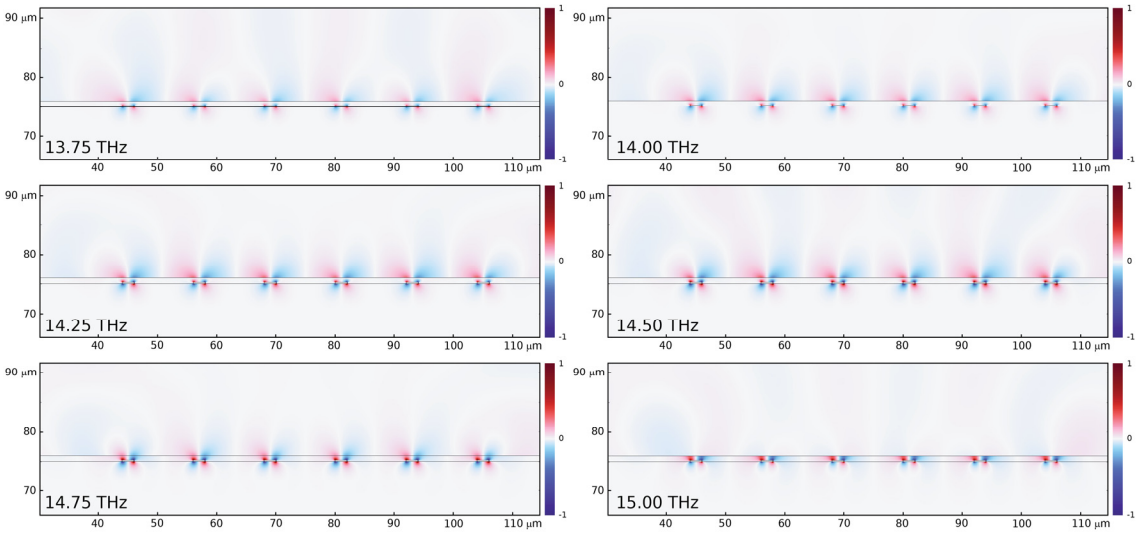

Figure S12. Distribution of the y component of the THz electric field near the electrodes of the SSBCD device in the first phonon-polariton region of amorphous SiO_2 (13.75 – 15 THz).

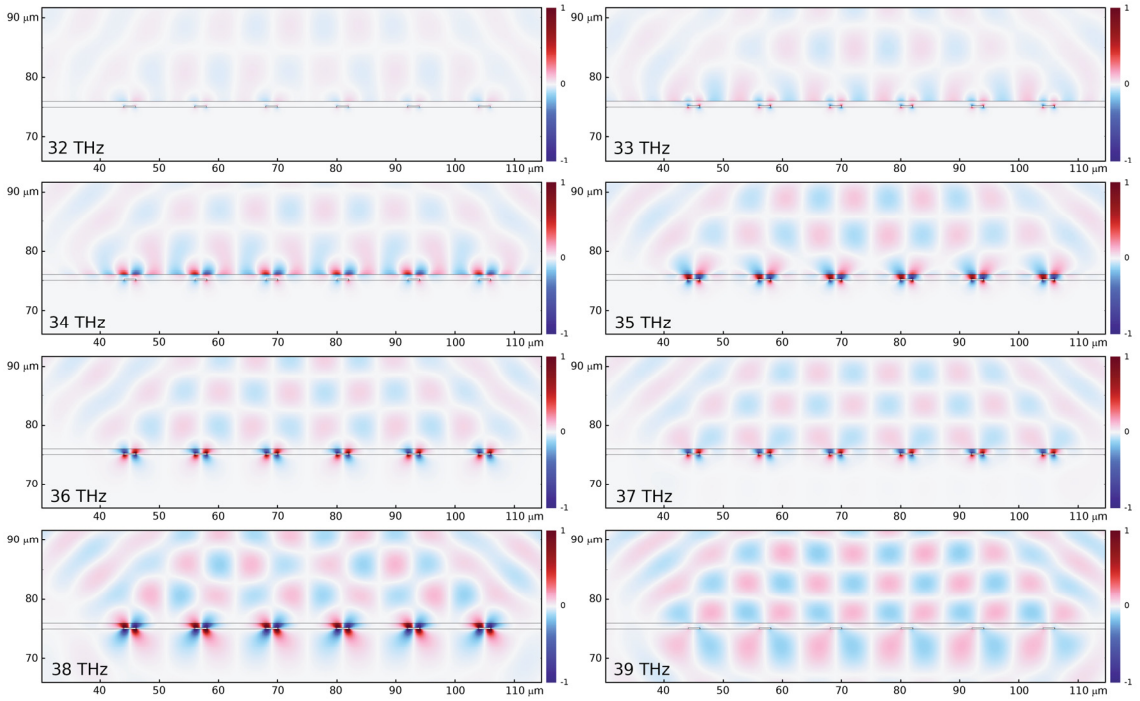

Figure S13. Distribution of the y component of the THz electric field near the electrodes of the SSBCD device in the second phonon-polariton region of amorphous SiO_2 (32 – 39 THz).

Secondly, at a frequency of 25 THz the spacing (12 μm) of the electrode matches the wavelength of the incoming radiation. Hence we see a very significant coupling between the electrodes, similar to the observations in the work of Walther *et al.* [13]. This is illustrated in Figure S14.

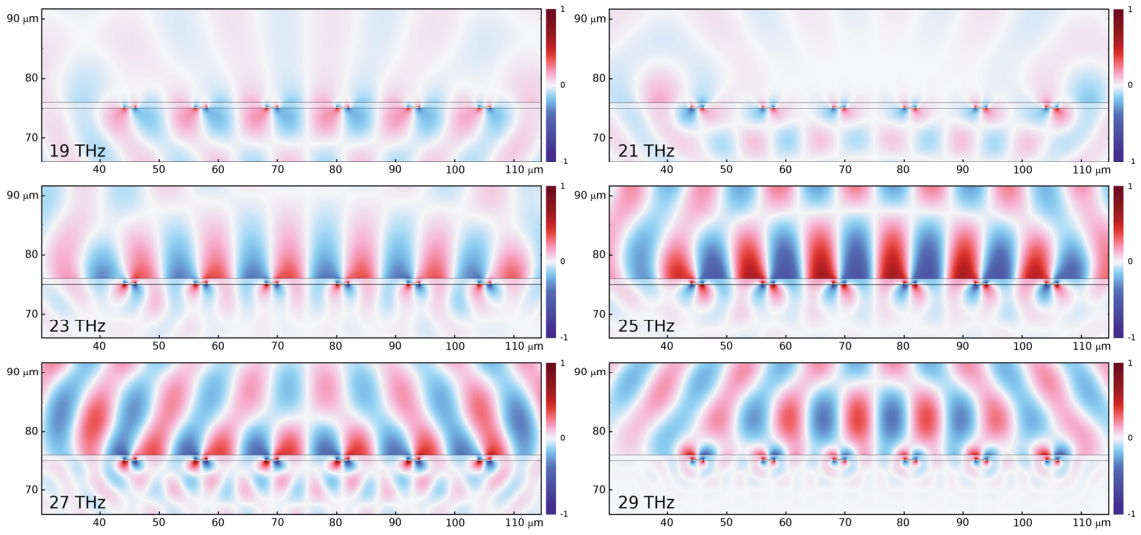

Figure S14. Resonant electromagnetic coupling between the electrodes. The electrode spacing (12 μm) corresponds to a resonant coupling at 25 THz in free space.

Supplementary references

[1] P. Sitz, and R. Yaris, "Frequency Dependence of the Higher Susceptibilities," J. Chem. Phys. **49**, 3546-3557 (1968).

[2] V. Mizrahi, and D. P. Shelton, "Dispersion of Nonlinear Susceptibilities of Ar, N_2, and O_2 Measured and Compared," Phys. Rev. Lett. **55**, 696-699 (1985).

[3] R. W. Boyd, *Nonlinear Optics* (Academic Press, Elsevier, 2008).

[4] A. V. Husakou, and J. Herrmann, "Supercontinuum Generation of Higher-Order Solitons by Fission in Photonic Crystal Fibers," Phys. Rev. Lett. **87**, 203901 (2001).

[5] P. U. Jepsen, D. G. Cooke, and M. Koch, "Terahertz spectroscopy and imaging – Modern techniques and applications," Laser Photon. Rev. **5**, 124-166 (2011).

[6] M. Born, and E. Wolf, *Principles of Optics: Electromagnetic Theory of Propagation, Interference and Diffraction of Light* (Cambridge University Press, 1999).

[7] D. Grischkowsky, S. Keiding, M. van Exter, and C. Fattinger, "Far-infrared time-domain spectroscopy with terahertz beams of dielectrics and semiconductors," J. Opt. Soc. Am. B **7**, 2006-2015 (1990).

[8] S. N. Taraskin, S. I. Simdyankin, S. R. Elliott, J. R. Neilson, and T. Lo, "Universal features of terahertz absorption in disordered materials," Phys. Rev. Lett. **97**, 055504 (2006).

[9] A. Tomasino, A. Mazhorova, M. Clerici, M. Peccianti, S.-P. Ho, Y. Jestin, A. Pasquazi, A. Markov, X. Jin, R. Piccoli, S. Delprat, M. Chaker, A. Busacca, J. Ali, L. Razzari, and R. Morandotti, "Solid-state-biased coherent detection of ultra-broadband terahertz pulses," Optica **4**, 1358-1362 (2017).

[10] A. Tomasino, R. Piccoli, Y. Jestin, S. Delprat, M. Chaker, M. Peccianti, M. Clerici, A. Busacca, L. Razzari, and R. Morandotti, "Invited Article: Ultra-broadband terahertz coherent detection via a silicon nitride-based deep sub-wavelength metallic slit," Apl Photonics **3**, 8 (2018).

[11] J. B. Tice, V. R. D'Costa, G. Grzybowski, A. V. G. Chizmeshya, J. Tolle, J. Menendez, and J. Kouvetakis, "Synthesis and Optical Properties of Amorphous Si3N4−xPx Dielectrics and Complementary Insights from ab Initio Structural Simulations," Chemistry of Materials **22**, 5296-5305 (2010).

[12] G. Cataldo, J. A. Beall, H.-M. Cho, B. McAndrew, M. D. Niemack, and E. J. Wollack, "Infrared dielectric properties of low-stress silicon nitride," Opt. Lett. **37**, 4200-4202 (2012).

[13] A. Bitzer, J. Wallauer, H. Merbold, H. Helm, T. Feurer, and M. Walther, "Lattice modes mediate radiative coupling in metamaterial arrays," Opt. Express **17**, 22108-22113 (2009).